nature communications

Article

https://doi.org/10.1038/s41467-025-58373-6

Oxide-dispersion-enabled laser additive manufacturing of high-resolution copper

Received: 26 September 2024

Accepted: 20 March 2025

Published online: 04 April 2025

Check for updates

Shuo Qu[1,10], Liqiang Wang[2,10], Shengbiao Zhang[3,10], Chenfeng Yang[4], Hou Yi Chia[5], Gengbo Wu[4,6], Zongxin Hu[1], Junhao Ding[1], Wentao Yan[5], Yang Zhang[7], Chi Hou Chan[4], Wen Chen[3,8] ✉, Yang Lu[9] ✉ & Xu Song[1] ✉

Laser additive manufacturing of pure copper (Cu) with complex geometries opens vast opportunities for the development of functional devices in microelectronics and telecommunication. However, laser additive manufacturing of high-resolution pure Cu remains a challenge. Here we report a facile oxide-dispersion-strengthening (ODS) strategy that enables additive manufacturing of Cu with sub-100 μm (~70 μm) resolution by laser powder-bed fusion. This ODS strategy starts with oxygen-assisted gas atomisation to introduce ultrafine Cu_2O nanoparticles into the pure Cu powder feedstock. These nanoscale dispersoids not only improve the laser absorptivity and the viscosity of the melt but also promote dynamic wetting behaviour. The ODS Cu exhibits a remarkable yield strength of ~450 MPa and a large uniform elongation of ~12%, while preserving a high electrical conductivity. As an example, we printed an ODS Cu micro-architected terahertz antenna, which demonstrates a 2.5-fold improvement in signal intensity compared with traditional 3D-printed pure Cu antennas.

The pursuit of three-dimensional (3D) complex copper (Cu) devices with high mechanical strength and electrical conductivity is vital for a broad range of applications, including tele-communication[1], electronics[2], and thermal management[3]. The recent advances in laser additive manufacturing (AM)[4,5], also called 3D printing, have enabled net-shaping of Cu components with complex geometries[6–8]. However, a significant challenge in laser AM of Cu lies in the difficulty of controlling printing defects, such as lack-of-fusion or keyhole pores, which are associated with the intrinsic physical properties of Cu–high infrared laser reflectivity and high thermal conductivity, which are very unfriendly to laser processing[9]. Hence, high-energy input is often required to fabricate dense and defect-free Cu components to compensate the energy loss due to laser reflection and heat dissipation[7]. To this end, short-wavelength (green or blue) laser beam sources, due to the increased absorptivity for Cu, have been widely adopted for laser AM of Cu components with high relative densities[1]. Nevertheless, increasing the energy absorption of Cu inevitably leads to severe material fusion and thus deteriorates the printing resolution, resulting in a trade-off between material density and printing resolution. In addition, the significant volume expansion and perturbation of the liquid melt pool of Cu under a high energy input give rise to a high surface roughness[10]. Thus far, the minimum feature size that can be achieved for laser AMed Cu is limited to 100–200 μm with a surface roughness of R_a ranging from 5

[1]Department of Mechanical and Automation Engineering, Chinese University of Hong Kong, Hong Kong SAR, China. [2]Department of Mechanical Engineering, City University of Hong Kong, Hong Kong SAR, China. [3]Department of Mechanical and Industrial Engineering, University of Massachusetts, Amherst, MA, USA. [4]State Key Laboratory of Terahertz and Millimeter Waves, Department of Electrical Engineering, City University of Hong Kong, Hong Kong SAR, China. [5]Department of Mechanical Engineering, National University of Singapore, Singapore, Singapore. [6]City University of Hong Kong Shenzhen Research Institute, Shenzhen, China. [7]School of Materials Science and Engineering, Shaanxi University of Technology, Hanzhong, China. [8]Department of Aerospace and Mechanical Engineering, University of Southern California, Los Angeles, CA, USA. [9]Department of Mechanical Engineering, The University of Hong Kong, Hong Kong SAR, China. [10]These authors contributed equally: Shuo Qu, Liqiang Wang, Shengbiao Zhang. ✉e-mail: wchen001@usc.edu; ylu1@hku.hk; xsong@mae.cuhk.edu.hk

to 20 µm[11], which impedes further development of the device performance.

Beyond the abovementioned density-resolution trade-off, the widespread application of laser AMed Cu components is particularly plagued with low mechanical strength. For example, the yield strength of pure Cu fabricated by laser-based powder-bed fusion (PBF-LB) is in the range of 200–300 MPa[6], which is comparable to but often lower than that of pure Cu from traditional wrought processing (up to ~365 MPa)[12]. Micro-alloying of Cu is a well-known metallurgical strategy to achieve an enhanced strength through solid-solution hardening, but the electrical conductivity of micro-alloyed Cu is much lower than pure Cu due to the high solubility of alloying elements that induces scattering effect of electrons[13]. The incorporation of immiscible ceramic nanoparticles, such as Y_2O_3[14,15], is also a typical strategy to reinforce Cu matrix during PBF-LB[7,16]. On one hand, common approaches often rely on ex-situ decoration of nanoparticles onto the surfaces of Cu powders, such as mechanical mixing[17], dielectrophoretic controlled adsorption[18], and acoustic mixing[19]. Although they are viable methods to enhance the yield strength of Cu, they suffer from undesired agglomeration of nanoparticles during powder mixing and/or melt solidification, resulting in limited improvement in mechanical properties[20]. For instance, due to segregation, the formation of a carbon-rich microstructure occurs in the pure Cu matrix, which can act as a crack initiator and further reduce mechanical properties rather than improve them[21]. On the other hand, controlling the atmosphere during the process of AM is also a viable method for in-situ formation of ODS particles, which provides oxygen to the melt pool by interaction between the melt and an oxygen-containing atmosphere. While it is an effective way of producing ODS particles, the AM process under reactive atmospheres encounters different kinds of challenges, such as temperature variation within melt pool, varying degrees of gas dissolution, and short interaction times between melt and atmosphere[22]. These preliminary studies suggest that achieving high resolution for AMed Cu devices without compromising their mechanical and functional properties remains a challenging task.

Here, we present a facile oxide-dispersion-strengthening (ODS) strategy to simultaneously enhance the laser absorptivity and improve the stability and wettability of the Cu melt, which leads to superb printing resolution and material properties of the AMed ODS Cu components. Similarly, in the laser welding process, which shares some common features with laser AM, oxygen can be used to modify the surface tension gradient and increase the penetration depth of the melt pool, reducing the transverse thermal diffusion and leading to improved laser weldability of metals[23]. Additionally, oxide dispersoids are also known as effective strengthening particles to improve the yield strength of metals[24]. Compared to conventional methods for fabricating ODS materials, oxide particles in the AMed alloys are more uniformly distributed and less agglomerated due to rapid solidification kinetics during AM, thereby further improving the mechanical properties. ODS alloys with Fe, Ni and Al as base matrices have been successfully manufactured through AM, exhibiting excellent mechanical properties[25]. Thus, ODS strategy shows great potential for laser AM of high-resolution Cu components with high strength. Unlike conventional ODS strategies that often mechanically introduce oxide particles onto the surface of powder feedstock, we introduce oxide nanoparticles to the Cu powder feedstock from the interior to the surface, through controlling the oxygen content during gas atomisation. This ODS strategy opens up the opportunities for a wide range of applications, such as the next-generation Cu micro-architected telecommunication devices enabled by laser AM. As a demonstrator, we fabricated an ODS Cu-based terahertz (THz) antenna with a 2.5-fold boost in gain, along with excellent radiation efficiency and bandwidth.

Results and discussion

Oxygen-assisted gas atomisation and laser powder-bed fusion

Figure 1A illustrates the PBF-LB process of ODS Cu with uniformly distributed oxide nanoparticles. We introduced the oxide nanoparticles into the Cu powder feedstock via OAGA process with precise control of the oxide content. By adjusting the oxygen partial pressure during gas atomisation, different oxygen contents (0.2, 0.4, 0.6 wt.%) of ODS Cu powder feedstock can be facilely achieved (see Supplementary Text 1 and Supplementary Fig. 1). The adjustable performances also demonstrate the controllability of ODS strategy to adapt to various practical requirements. In this study, ODS Cu with 0.4 wt.% oxygen content is selected for thorough investigation due to its advantageous combination of high mechanical strength and electrical conductivity (Supplementary Fig. 1). The oxide phase in the ODS Cu powders and the as-printed component is both identified as Cu_2O by X-ray diffraction (XRD) (Supplementary Fig. 2 and Methods). Because oxygen has an low solubility in the Cu matrix[26], it exists mainly in the form of oxide nanoparticles both on the powder surface (region I) and in the powder interior (region II) (Fig. 1B–D), and avoids undesirable agglomeration compared to mechanical mixing. The gas atomisation process typically experiences a cooling rate in the range of 10^4–10^6 K/s[27], facilitating the formation of highly refined Cu_2O nanoparticles with an approximate size of 100 nm in the Cu matrix of the powder feedstock (Fig. 1D). For comparison, the microstructure of pure Cu powder is shown in Supplementary Fig. 3. In Fig. 1E, the close-up view of the melt pool shows that when the laser beam interacts with the powder bed, the melt pool undergoes transient heat transfer, complex multiphase flow, and rapid solidification, which are affected by multifaceted physical phenomena including surface tension gradient, Marangoni convection, and vapor recoil[28].

The parameters of laser AM are listed in Supplementary Table 1, which result in the same normalised enthalpy ($\Delta H/h_s$) [24, 25], determined by the laser processing parameters and the thermophysical properties of the material (see Supplementary Text 2 for details). Therefore, the as-printed ODS Cu exhibits a highly heterogeneous microstructure characterised by multiscale structural features spanning four orders of magnitude in length scale, from tens of micrometres down to nanometres (Fig. 2A–F). At the microscale, optical microscopy and electron backscatter diffraction (EBSD) reveal a nearly random crystallographic texture and a heterogeneous grain structure for ODS Cu, with the grain size ranging from hundreds of nanometres to tens of micrometres. The average grain size of the as-printed ODS Cu is ~4 µm (Fig. 2A, B and Supplementary Fig. 4), which is approximately half that of the as-printed pure Cu (~8 µm, Supplementary Fig. 5). Notably, many nano-sized equiaxed grains are visible in the as-printed ODS Cu (Fig. 2B). Magnified bright-field transmission electron microscopy (TEM) images confirm the presence of these ultrafine equiaxed grains (Fig. 2C). Notably, the Cu_2O nanoparticles with a volume fraction of ~1.1% (detected by high-energy synchrotron XRD, see Methods), are uniformly distributed in the Cu matrix (Fig. 2D and Supplementary Fig. 6). During laser melting, the dispersion of oxide nanoparticles in the pure Cu matrix is driven by particle flow. To achieve uniform dispersion, vapor suppression and the Marangoni convection effect are particularly important[28]. Most nanoparticles appear in a near-spherical shape with an average diameter of ~15 nm (Fig. 2D, E). The high-resolution transmission electron microscopy (HRTEM) image demonstrates that the lattice misfit at the phase interface between the (111) Cu_2O and (111) Cu crystal planes is 15.3% (Fig. 2F). Furthermore, the thin-wall sample of ODS Cu was also characterised using EBSD and TEM, as shown in Supplementary Figs. 7 and 8, because the thermal history of thin walls produced by PBF-LB differs significantly from that of bulk material. The microstructure of the thin walls is nearly dense, with an average grain size of approximately 6.25 µm, which is slightly larger than that of bulk samples. This difference arises because the thin walls undergo fewer remelting cycles and have a consistent thermal gradient direction, leading to the

https://doi.org/10.1038/s41467-025-58373-6

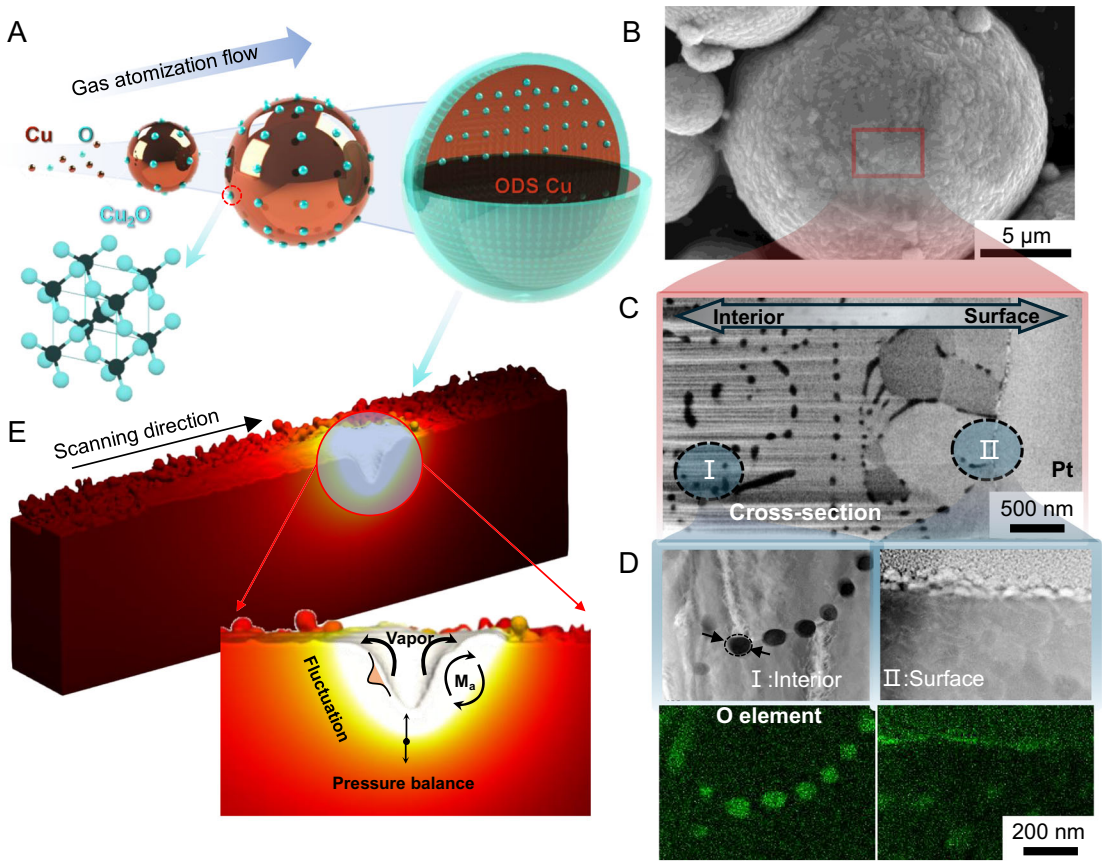

Fig. 1 | ODS-enabled laser AM of Cu. A Schematic of ODS Cu powder feedstock prepared by OAGA approach in this work. **B** Surface morphology of ODS Cu powder. **C** Cross-sectional morphology of ODS Cu powder from interior to surface. **D** Close-up views and oxygen elemental maps of interior (region I) and surface (region II) of ODS Cu powder. **E** Schematic of the PBF-LB process.

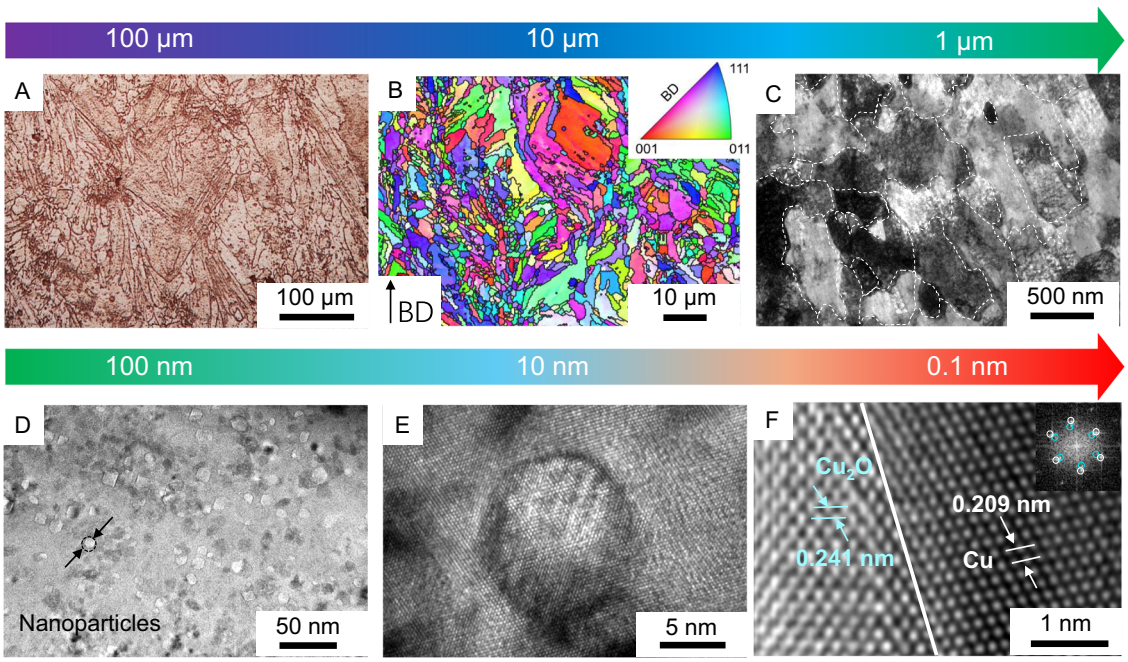

Fig. 2 | Microstructure of ODS Cu. A, **B** Optical microscopy and EBSD grain orientation map of the as-printed ODS Cu sample, respectively. BD: build direction. **C** TEM image of ultrafine equiaxed grains. **D** Cu_2O nanoparticle distribution in the as-printed ODS Cu. **E** High-magnification of a typical Cu_2O nanoparticle with a spherical morphology in the matrix. **F** HRTEM image showing the atomic-level Cu/Cu_2O phase interface with the insets showing the corresponding Fast Fourier Transform (FFT) diffractogram of the interface area.

https://doi.org/10.1038/s41467-025-58373-6

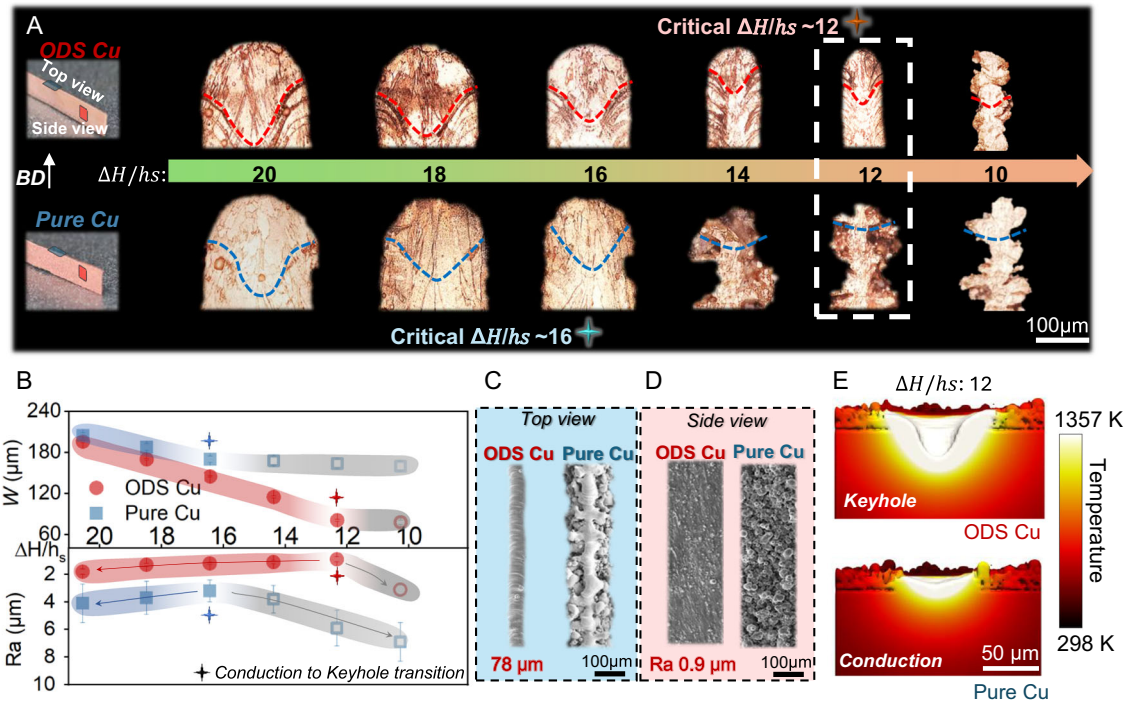

Fig. 3 | Comparison of AMed ODS Cu and Pure Cu in printing resolution and melt behaviour. A Side cross-sectional morphologies of melt pools. The dashed lines represent the boundaries of the molten pools. **B** Track line resolution and surface roughness printed with different normalised enthalpy ($\triangle H/h_s$) values. Comparison of **C** top surface morphologies and **D** side surface morphologies of thin walls using a low $\triangle H/h_s \approx 12.3$. **E** Side cross-sectional morphologies of high-fidelity melt pool simulations.

formation of columnar grains as shown in Supplementary Fig. 8A. In contrast, the thermal gradient direction for bulk samples is more complex during the printing process due to the 67° rotation angle between layers. On the other hand, the average nanoparticle size is around 15 nm, identified as Cu_2O phase by EDS analysis. Moreover, Cu_2O is distributed uniformly within the grains, consistent with observations in bulk samples. The Cu_2O microstructure of thin walls is identical to that of bulk samples, indicating that the intrinsic heat treatment induced by laser scanning has minimal effect on the nanoparticles. Overall, this demonstrates that the Cu_2O nanoparticles introduced by the ODS strategy play a pivotal role in modifying the solidification microstructure of Cu during PBF-LB.

The above XRD and microstructural observations suggest that Cu_2O is the main nanoprecipitation phase in ODS Cu, both in the gas-atomised powders and in the as-printed material after PBF-LB. Yet, the average size of the Cu_2O nanoparticles is reduced by almost an order of magnitude, from ~100 nm in the starting ODS Cu powder feedstock to ~15 nm in the as-printed ODS Cu. During PBF-LB, the temperature within the melt pool can rise up to 3000 K, well above the melting point of Cu_2O (1505 K)[29]. Thus, the Cu_2O nanoparticles are expected to undergo melting and re-precipitation upon rapid solidification of the melt pool. The significantly refined Cu_2O nanoparticle size largely arises from the high cooling rate of 10^6–10^7 K/s during PBF-LB[30]. Note that the CuO phase was neither present in the initial ODS Cu powder feedstock nor in the AMed material. This is likely attributed to the following facts: (1) CuO's asymmetric crystal structure is less stable than the cubic structure of Cu_2O at nanoscale[31]; (2) Cu_2O is the initial phase in the sequential two-step oxidation process of Cu[29], and the second step of oxidation, from Cu_2O to CuO, may be kinetically suppressed during rapid solidification of both the gas atomisation and PBF-LB processes.

Achieving high-resolution PBF-LB of ODS Cu

Printing resolution is a key aspect of the 3D printing process, as it directly limits the design features of the printed object[32]. In this work, the normalised enthalpy ($\Delta H/h_s$), which is determined by the correlation between the energy absorbed by the laser at a certain volume and the extent of the enthalpy change in the liquid phase, is used to analyze the melting behaviour of ODS Cu with that of pure Cu (Supplementary Text 2). The use of normalised enthalpy in evaluating the melting process is advantageous because it combines the thermophysical properties, scan speed, and laser power into a single factor. This factor not only differentiates conduction and keyhole modes, but also predicts the resulting size and shape of the melt pool for a broader range of operating parameters[33]. To achieve finer features via PBF-LB, the melt track should be narrow, which is usually achieved at reduced laser energy inputs (i.e., low $\Delta H/h_s$ values). However, low $\Delta H/h_s$ inputs during pure Cu fabrication tend to result in the formation of various printing defects including pores, cracks, unmelted powders, and poor adhesion to the previous layer[34]. Thus, the tradeoff between printing resolution and material density indicates a critical value of $\Delta H/h_s$ that instigates the optimum attainable resolution of dense components.

Here, the printing resolution of ODS Cu is compared with that of pure Cu, evaluated using two descriptors: (i) melt track width and (ii) surface roughness of a thin-wall structure fabricated by laser scanning of single tracks layer by layer. The cross-sectional morphologies of thin walls can easily demonstrate the melt pool shape and the side-surface contour (ODS Cu vs pure Cu) under varying $\Delta H/h_s$ values (Fig. 3A). The PBF-LB of ODS Cu offers a significantly improved resolution when compared with pure Cu, as reflected by the minimum attainable melt track width (W) with smooth contours; W of the ODS Cu sample achieves a minimum value of 78 μm at $\Delta H/h_s \approx 12$, while W of the pure Cu sample achieves a minimum value of 160 μm at $\Delta H/h_s \approx 16$ (Fig. 3B). The error bars represent standard deviations derived from the measurements of three repeated samples. The shaded region clearly illustrates the variation trend of the melt pool. Specifically, the red (ODS Cu) and blue (pure Cu) areas signify the keyhole mode, while the grey area denotes the conduction mode. Any further decrease in $\Delta H/h_s$ below the critical values leads to irregular and discontinuous

https://doi.org/10.1038/s41467-025-58373-6

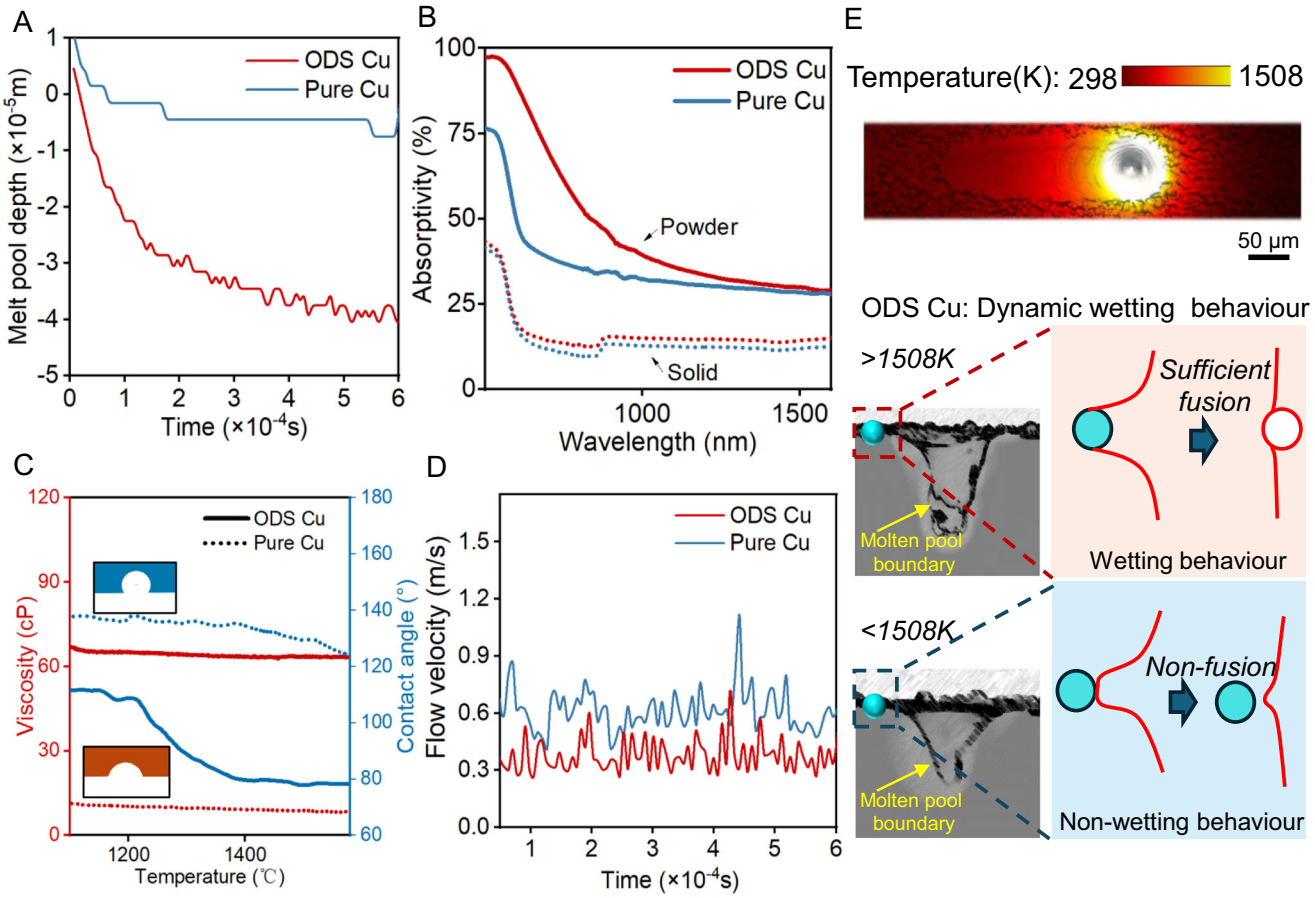

Fig. 4 | High-resolution printing mechanism of ODS Cu. High-fidelity melt pool simulations: **A** Melt pool depth. **D** Liquid flow velocity. Thermophysical properties of ODS Cu and pure Cu: **B** Laser absorptivity. **C** Viscosity and contact angle. **E** Experimental validation and simulation of the dynamic wetting behaviour of ODS Cu.

morphologies of the thin walls, despite the decrease in melt track width. This type of defect manifests due to the so-called balling effect at ultralow energy inputs and is not considered a satisfactory deposit. In terms of surface roughness (R_a), pure Cu printed under a lower $\Delta H/h_s$ results in a substantial increase in R_a from 3 μm to 8 μm. Conversely, ODS Cu demonstrates improved R_a consistently compared with pure Cu and exhibits an optimal R_a of ~0.9 μm at the critical normalised enthalpy input. As depicted in Fig. 3C, the morphologies of thin walls fabricated under $\Delta H/h_s \approx 12$ (ODS Cu: at critical value vs pure Cu: below critical value) exhibit a notable difference between ODS Cu and pure Cu. The top views further reveal the difference in resolution between ODS Cu and pure Cu at low $\Delta H/h_s$. The discontinuity of pure Cu melt track and the adhered powders lead to larger W in comparison to ODS Cu. Additionally, the difference in R_a is evident in the side views, where the sintered powder particles formed by lack-of-fusion in pure Cu worsen surface roughness (Fig. 3D). By contrast, the side surface of ODS Cu track exhibits a powder-free morphology.

To further elucidate the mechanistic origin of different printing resolutions between Cu and ODS Cu, we probed the melt pool dynamics using high-fidelity melt pool simulations (Fig. 3E), supplemented by experimental measurements of fluid properties and direct observations. We identified three factors that can help improve printing resolution and surface roughness: (1) a narrow melt pool in stable keyhole mode at low normalised enthalpies, (2) increased stability of the melt pool, and (3) reduced powder adhesion/sintering, as discussed in detail below.

Firstly, the improvement in printing resolution is mainly attributed to the stable keyhole melting mode of ODS Cu under low normalised enthalpies. The melt pool boundaries of ODS Cu and pure Cu are highlighted by the red and blue curves, respectively, in Fig. 3A, and the corresponding aspect ratios of the two types of melt pool samples are shown in Supplementary Fig. 9. We observe that thin walls with smooth contours generally exhibit a deep melt pool, suggesting a keyhole melting mode. Therefore, the results indicate that the stable keyhole melting mode is beneficial for interlayer consolidation, which can be denoted by the critical $\Delta H/h_s$ for the transition point from conduction to keyhole mode. It is also observed that ODS Cu has a higher propensity to enter the stable keyhole mode than pure Cu under the same $\Delta H/h_s$. This behaviour is also corroborated by our high-fidelity simulations, where the melt pool of ODS Cu is five times deeper than that of pure Cu under the same $\Delta H/h_s$ (Figs. 3E and 4A). Such a more-stable keyhole melting mode of the ODS sample is attributed to its higher laser absorptivity of 37% compared to 31% for the pure Cu sample (see Supplementary Text 3 for more details), as measured by spectrophotometer at the wavelength of 1070 nm (Fig. 4B and Methods). The as-printed solid samples shown in Fig.4B verify the effectiveness of both the surface oxides and internal nanoparticles. It is known that the values obtained through spectrophotometry may not accurately represent laser-material interactions during PBF-LB. In addition, the melt mode is also a significant factor for the absorptivity of melt pool. The keyhole allows the laser to penetrate deeper into the material and leads to multiple reflections, considerably increasing absorptivity. Hence, we conducted the melt pool characterisations as shown in Fig. 3A to directly exhibit the melt pool conditions, such as depth, width and stability. Based on the absorptivity measurements and experimental analysis, we can deduce that the absorptivity of the ODS Cu melt is higher than that of pure Cu.

Moreover, although the surface tension of Cu is lowered by the presence of oxygen[35], it does not reverse Marangoni flow (Supplementary Fig. 10) and the decreased Marangoni number (*Ma*), induced by the higher viscosity of melt liquid, limits the widening of the melt pool. On the other hand, a higher $\Delta H/h_s$ is required for pure Cu to achieve a stable keyhole mode, which also leads to a wider melt pool. Thus, it is challenging for the pure Cu sample to attain narrow melt pools without compromising interlayer consolidation. Overall, PBF-LB of ODS Cu simultaneously achieves a narrow melt pool with stable keyhole melting behaviour under low $\Delta H/h_s$, which enables the manufacturing of Cu at sub-100 μm resolution.

Moreover, due to the high thermal conductivity and low viscosity of Cu, small perturbations or instabilities of the melt pool can readily occur and be instantaneously captured by the solidification front, thereby deteriorating the surface roughness of the printed material. In addition to the stable keyhole mode, the introduction of oxides further reduces the fluid perturbations by increasing the viscosity of ODS Cu melt from ~8 cP to ~64 cP due to the presence of Cu-O complex, measured by the oscillating-cup method (Fig. 4C and Methods, see Supplementary Text 4 for details)[36]. The simulations reveal a lower average flow velocity of the ODS Cu melt pool (0.37 $m{\cdot}s^{-1}$) than that of the pure Cu melt pool (0.66 $m{\cdot}s^{-1}$) (Fig. 4D), thus effectively reducing the fluctuation of melt pool. As a result, the increase in viscosity of the ODS Cu melt helps stabilise the melt pool, therefore improving the final surface roughness.

Lastly, the surface roughness improvement can be also attributed to the reduction of powder adhesion/sintering on the melt track surface, mainly due to two factors: (1) vapour plume blowing away powder under stable keyhole mode[37]; and (2) favourable dynamic wetting behaviour of liquid ODS Cu. Figure 4C compares the contact angle measured at different temperatures between Cu and ODS Cu. ODS Cu shows a lower contact angle than pure Cu at temperatures around the melting point, while the current contact angle is higher than 90°, exhibiting non-wetting behaviour similar to pure Cu. Furthermore, at temperatures exceeding 1235 °C, the contact angle decreases even further. This is because the presence of Cu-O complexions in the melt, which originates from Cu_2O, could reduce the solid/liquid interfacial energy due to the adsorption effect[38]. Particularly, the increasing oxygen content leads to a lower contact angle in ODS Cu after the melting of Cu_2O. Finally, at higher temperatures, the contact angle of ODS Cu (~80°) is lower than that of pure Cu (~130°) at 1600 °C, which enhances wetting and adhesion with the previous track and layer. Yet, wetting behaviour often leads to adjacent powder particles being dragged into the melt pool via surface tension. Because of insufficient heat at the melt pool track, the newly incorporated particles cannot be completely melted, resulting in partially melted particles adhering to the melt track edges (Fig. 3C), as is commonly observed in PBF-LB. However, the wetting behaviour of ODS Cu transitions into non-wetting upon solidification, which is often called dynamic wetting behaviour[39,40]. Therefore, neighbouring particles are less susceptible to being dragged into the melt track, as validated by both the experiments and simulation (Fig. 4E). Hence, we conclude that this dynamic wetting behaviour (see details in Supplementary Text 5) contributes to the smooth surface of ODS Cu. Overall, pure Cu by laser additive manufacturing suffers from microstructural defects and rough surface due to its low infrared absorptivity, low melt viscosity and non-wetting behaviour. In comparison, ODS Cu possesses the intrinsic thermophysical properties that facilitate the formation of narrow yet stable melt pools during PBF-LB without compromising surface quality, thus enabling it to achieve sub-100 μm resolution in PBF-LB.

Mechanical and electrical properties of ODS Cu

Figure 5A–E provide a thorough comparison of the electrical and mechanical properties of ODS Cu and pure Cu samples fabricated at their respective critical $\Delta H/h_s$ values. Pure Cu samples exhibit a near-maximum electrical and thermal conductivity of ~390 W/m·K (~96% IACS) due to their almost impurity-free composition. ODS Cu samples possess an electrical and thermal conductivity of ~320 W/m·K (~80% IACS) (Fig. 5A). The error bars indicate standard deviations calculated from three replicate measurements. The high conductivity of ODS Cu, with only a minor sacrifice in comparison to pure Cu, can be primarily attributed to the remarkably low solubility of oxygen in Cu. This observation is supported by the 3D tomographic reconstruction (showing nearly spherical morphology) and the proximity histogram of chemical composition (Cu and O elements) derived from one of the Atom Probe Tomography (APT, see Methods) datasets of the ODS Cu (Fig. 5B, C). Besides, the Cu-O elemental composition ratio of oxides at 2:1 further confirms that the nanoparticle phase consists of Cu_2O.

Figure 5D illustrates the tensile stress-strain curves of the PBF-LB ODS Cu and pure Cu bulk samples (see Methods) compared with other state-of-the-art 3D-printed nanoparticle-reinforced Cu and Cu-O alloy counterparts. Our ODS Cu exhibits a high yield strength of ~450 MPa, which is more than twice that of pure Cu (~200 MPa). Moreover, the ODS Cu demonstrates remarkable strain hardening, resulting in a substantial uniform elongation (UE) of 11.5% and a high ultimate tensile strength (UTS) of 524 MPa, significantly surpassing the strength-ductility combinations of other AMed Cu-O alloys and LaB_6-Cu nanocomposites reported recently[7,20,41]. Although pure Cu has a higher UE of 18.6%, ODS Cu with a UE exceeding 10% can still meet the requirements of most applications due to the net-shaping characteristic of 3D printing, as opposed to traditional manufacturing processes. As a result, our ODS Cu, benefitting from the Cu_2O nanoparticles and low oxygen solubility, displays unprecedented mechanical properties and satisfactory electrical conductivity (Fig. 5E and Supplementary Table 2)[42–54]. To assess the overall performance of Cu, the product of yield strength and electrical conductivity is adopted as a key performance indicator. Typically, most Cu/Cu alloys have the product values below the threshold of 15 GPa·%IACS, as delineated by the contour line in Fig. 5E. The incorporation of nanoparticles such as LaB_6 and oxides into the Cu matrix can push this value beyond the 15 GPa·%IACS threshold. Notably, our ODS Cu demonstrates a clear improvement in the product of yield strength and electrical conductivity without post-treatment, exceeding 35 GPa·%IACS, as highlighted in Fig. 5E.

The high yield strength of ODS Cu can be attributed to significant obstacles to dislocation motion, which include grain boundaries, printing-induced pre-existing dislocations, and Cu_2O nanoprecipitates[55,56]. Heterogeneous nucleation in ODS Cu, triggered by Cu_2O nanoprecipitates, results in substantially refined grain size (~4 μm) and high dislocation density (3.5×10^{14} m^{-2}) in ODS Cu, compared to 8 μm and 1.5×10^{14} m^{-2} for pure Cu. Based on classical strengthening laws, as discussed in Supplementary Text 6, the yield strength contributions from grain boundary hardening and dislocation hardening in ODS Cu are estimated to be 55 MPa and 142 MPa, respectively, far surpassing those in pure Cu (39 MPa and 93 MPa, respectively). In comparison, the Cu_2O nanoprecipitates contribute most significantly to the yield strength in ODS Cu through the Orowan strengthening mechanism (Supplementary Text 6), accounting for approximately half of the overall yield strength. In this work, Orowan bypass strengthening is the primary mechanism for these Cu_2O nanoprecipitates due to their semi-coherent interfaces with the Cu matrix (Fig. 2F), as evidenced by frequently observed dislocation pileups and entanglements in the vicinity of the Cu_2O precipitates (Supplementary Fig. 11 and Fig. 5F). The edge dislocation density near these Cu_2O nanoprecipitates is relatively low before deformation, as signified by the Inverse Fast Fourier Transform (IFFT) micrograph utilising the (111) FCC diffraction spots (Supplementary Fig. 11). With strain up to 15%, a number of edge dislocations are visible at the Cu-Cu_2O interfaces, while the Cu_2O nanoprecipitates remain elastic. According to the Orowan bypass mechanism, increasing particle content can result in higher yield strength. Hence, increasing the

https://doi.org/10.1038/s41467-025-58373-6

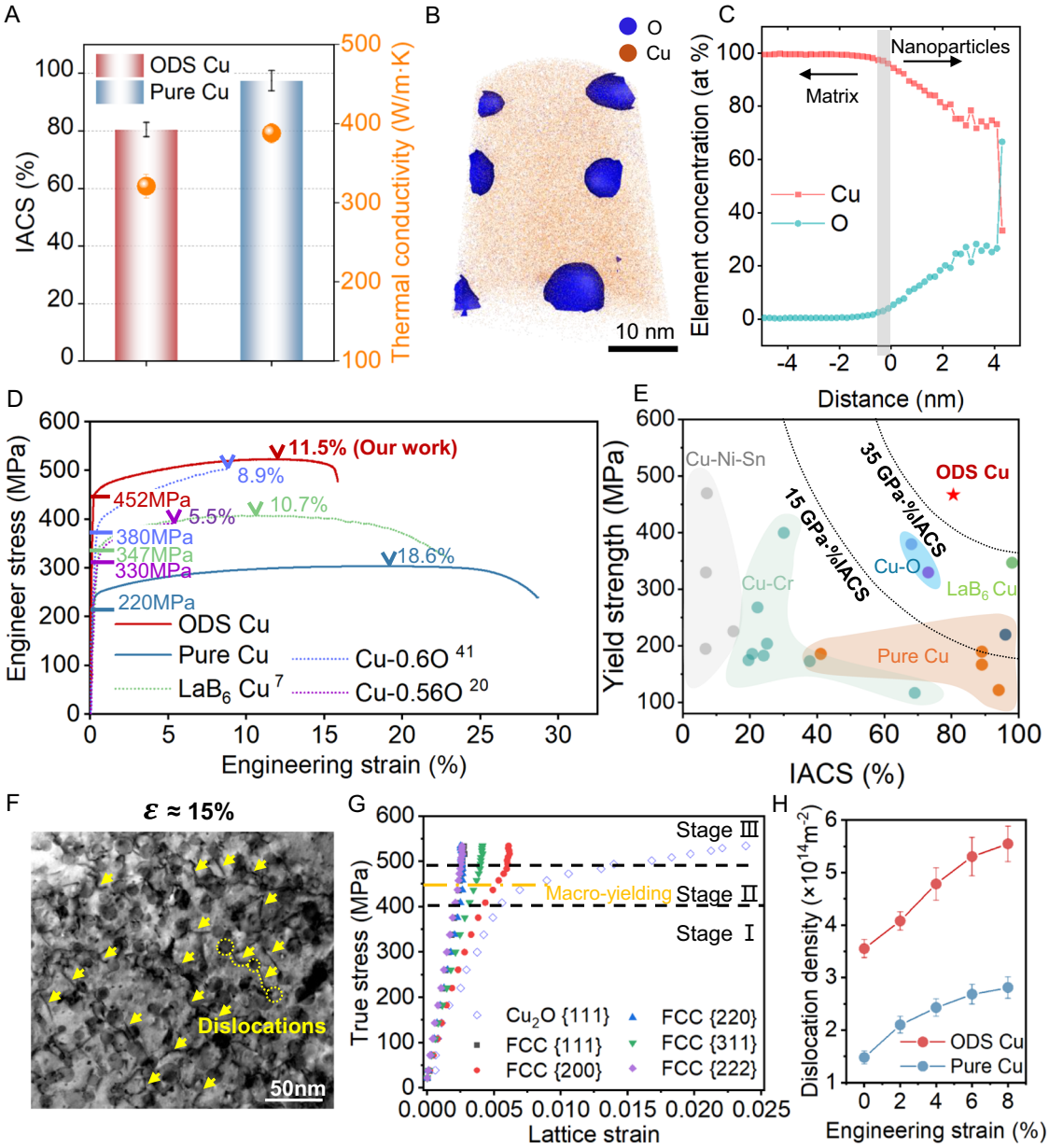

Fig. 5 | Mechanical and electrical properties of AMed ODS Cu and pure Cu. **A** Electrical conductivity and thermal conductivity of AMed ODS Cu and pure Cu. Atom probe tomography (APT) characterisation of AMed ODS Cu: (**B**) 3D tomographic reconstruction; (**C**) Elemental distribution across the Cu/Cu_2O phase interface. **D** Tensile stress-strain curves of AMed ODS Cu in this work in comparison with state-of-the-art 3D-printed nanoparticle-reinforced Cu and Cu-O alloys from the literature[7,20,41]. **E** Comparison of yield strength and electrical conductivity of our AMed ODS Cu with previously reported Cu and Cu alloys produced by PBF-LB[42–54]. **F** BF-TEM image obtained under the two-beam condition, revealing the presence of dislocations (yellow arrows) and dislocation loops (dashed yellow circles) in plastically deformed AMed ODS Cu at 15% strain. **G** Evolution of lattice strain with macroscopic applied stress for representative Cu matrix (including FCC-{111}, {200}, {220}, {222} and {311}) and Cu_2O {111} crystallographic plane families along the loading direction. The macroscopic yield strength is indicated by the orange dashed line for reference. **H** Dislocation density evolution during deformation of the AMed ODS Cu and pure Cu.

volume fraction of precipitates, controlled by oxygen content, is an effective and facile approach to potentially further improving the yield strength of ODS Cu, as demonstrated in our work (Supplementary Fig. 1).

We further investigated the mechanistic origin of the high strain-hardening capacity of the ODS Cu using in-situ synchrotron X-ray diffraction (SXRD), which enables quantitative measurement of internal stress partitioning between the two constituent phases during loading. Figure 5G illustrates the lattice strain ε_{hkl} (see Method) along the loading direction, plotted against the macro true stress (σ), for the representative {*hkl*} crystallographic families of the face-centered cube (FCC) Cu matrix and the Cu_2O nanoprecipitates. Specifically, three deformation stages are evident. In stage I ($\sigma < 400$ MPa), both the Cu and Cu_2O phases undergo elastic deformation, with varying diffraction elastic constants due to the elastic anisotropy of individual grain families. Moving to stage II ($\sigma \approx 400$–490 MPa), all Cu and Cu_2O reflections deviate from the linear trend line. At ~400 MPa, both the Cu {220} and Cu_2O {111} lattice strains start to shift downwards due to the load shedding from the plastically deformed Cu grain families such as {111}, {220} and {222}, indicating the onset of plastic macro-yielding. In stage III ($\sigma > 490$ MPa), the lattice strains of all Cu grain families shift upward. In contrast, the lattice strain evolution of Cu_2O {111} grain turns downward, indicating that Cu_2O elastically takes on an additional load, which is relaxed through plastic deformation of the Cu phase.

The elastically deformed Cu_2O reflection is consistent with the TEM observations, suggesting that oxide particle cutting or shearing is not the operative mechanism in ODS Cu.

To further investigate the deformation mechanisms, we examined the dynamic evolution of the dislocation density through SXRD measurements using the modified Williamson-Hall approach[57]. As shown in Fig. 5H, ODS Cu demonstrates a more rapid increase in dislocation density during plastic deformation, rising from approximately $3.5 \times 10^{14}\,m^{-2}$ to $5.5 \times 10^{14}\,m^{-2}$, in contrast to pure Cu, where the dislocation density increases from ~$1.5 \times 10^{14}\,m^{-2}$ to only ~$2.8 \times 10^{14}\,m^{-2}$. The remarkable increment of dislocation density in ODS Cu is directly linked to the presence of the profuse and uniformly distributed Cu_2O nanoprecipitates, which promote dislocation multiplication and storage, leading to the pronounced work hardening of the ODS Cu via the Orowan bypass strengthening effect.

We conducted a thorough investigation of the matrix-nanoparticle interfaces using HRTEM, as depicted in Fig. 5F, to verify the dislocation density evolution. This microstructural observation substantiates the effective storage of dislocations at the Cu-Cu_2O phase interfaces. Essentially, the matrix-nanoparticle interfaces effectively impede and retain dislocations, thereby contributing to the remarkable synergy of high strength and stain hardening in ODS Cu. Furthermore, the presence of dislocations and dislocation loops revealed in the bright-field transmission electron microscopy (BF-TEM) image serves to further explain the Orowan bypass mechanism (Fig. 5F). Overall, the nanoscale Cu_2O particles in ODS Cu offer a pronounced enhancement of mechanical properties without a notable decrease in conductivity. Our results suggest that the ODS Cu shows great potential for practical applications, such as heat sinks/exchangers and antennas, which often demand high resolution and high mechanical strength, as well as high electrical and thermal conductivity.

AMed ODS Cu in transmit-array antenna application

In the upcoming 6 G communication systems, the THz band offers the capability to penetrate partial occlusions, enabling high-precision imaging and perception in non-visual scenes. Hence, THz communication systems are expected to be deployed on satellites, drones, airships, and other aerial- and space-based platforms as wireless communication and relay equipment to enable integrated air–space–land–sea communication[58]. These diverse and harsh environments often require robust mechanical properties to ensure accurate transmission during vibration and impact. By combining high-resolution printing with high strength and electrical conductivity, we demonstrate the superiority of our 3D-printed ODS Cu in the fabrication of micro-architected devices for advanced telecommunications.

For the demonstration case, the ODS Cu THz transmit-array antenna consists of an array of antenna elements that control the transmission phase, with the waveguide serving as the fundamental antenna element (Fig. 6A). The enlarged view of the single wall in the lattice is presented to show the high-resolution feature size in the inset

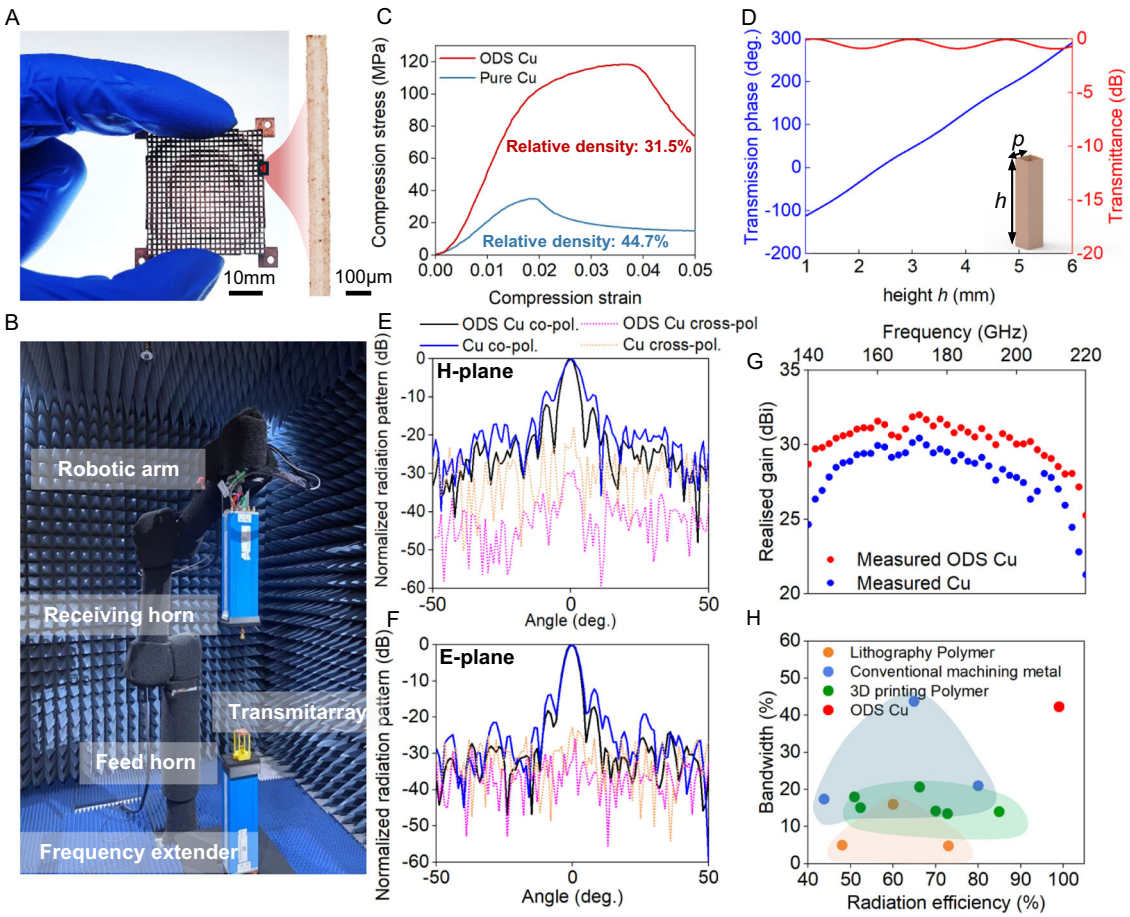

Fig. 6 | Characterisation and functional performance of ODS Cu-based THz transmit-array antenna. A As-printed transmit-array antenna samples using ODS Cu, and the zoom-in view of the lattice in the inset. **B** Compression stress–strain behaviour of the lattice components derived from THz antenna design fabricated by ODS Cu and pure Cu. **C** Antenna measurement setup in the anechoic chamber. **D** Simulated transmit-array element performance against height at 150 GHz. The inset represents the fundamental antenna element. Measured radiation patterns of the transmit-array antennas at the (**E**) H-plane and (**F**) E-plane. **G** Measured realised gain of the transmit-array antennas. **H** Comparison of bandwidth and radiation efficiency with previously reported antennas.

of Fig. 6A. Well-designed antenna elements allow the transmit-array to compensate for spatial phase delays originating from the feed source, creating a uniform phase distribution over the radiating surface. The lattice size of the waveguide was set at 0.7 λ_0 (where λ_0 is the free-space wavelength at 150 GHz), with a wall thickness of 100 µm. As-fabricated antennas using ODS Cu and pure Cu are shown in Supplementary Fig. 12 to illustrate the difference in printing resolution, with the ODS Cu lattice exhibiting a yield strength three times higher than the pure Cu lattice and simultaneously offering a 30% weight reduction (Fig. 6B). The experimental setup for antenna performance is shown in Fig. 6C, and the desired phase distribution is displayed in Supplementary Fig. 13. The element height h was varied from 1 mm to 6 mm to achieve 360° coverage of the transmission phase at 150 GHz (Fig. 6D).

Notably, ODS Cu enabled the creation of thin walls with varying heights without the need for machining or post-treatment, eliminating the high costs and high defect rates associated with conventional methods. Figure 6E and F display the measured radiation patterns generated by the two transmit-array antennas made from ODS Cu and pure Cu. The cross-polarisation level of the ODS Cu antenna was −31.1 dB, substantially lower than that of the pure Cu antenna (-22.8 dB), indicating significantly improved radiation efficiency. Additionally, the sidelobes (black lines) of the ODS Cu antenna were smaller than those of the pure Cu antenna (blue lines) in both the E- (the plane defined by the electric field vector) and H- (the plane defined by the magnetic field vector) planes. This improvement is attributed to the lower surface roughness walls of ODS Cu, resulting in superior multichannel communication performance with reduced disturbances. In the investigated frequency range from 140 to 220 GHz, the largest gain discrepancy was ~4 dB at 204 GHz, with the ODS Cu antenna (30.6 dBi) producing 2.5 times the signal intensity of the pure Cu antenna (Fig. 6G). This resulted in a wide bandwidth from 149 to 188 GHz (1.5 dB gain ~23.2%; 3 dB gain >43%) and high radiation efficiency (>99%), as expected.

Figure 6H shows that the ODS Cu antenna outperformed other THz antennas in terms of the radiation efficiency and bandwidth (see details in Supplementary Table 3)[59–68]. Notably, 3D printing techniques for dielectric materials, such as polymers, have been developed owing to the processing simplicity and cost-effectiveness. However, the surface wave effect induced by dielectric material leads to significant energy dissipation and reduced antenna radiation efficiency as the operating frequency approaches the THz range[64]. Although post-treatment techniques, such as surface metallisation, can be introduced, they increase resistivity and cost, and also limit design freedom[69]. Furthermore, conventional machining cannot process complex internal features during post-processing. Consequently, antenna design options are often constrained by traditional processes, which often ended up improving one attribute and scarifying another. In contrast, our 3D-printed ODS Cu offers multiple advantages simultaneously: (1) high mechanical robustness, (2) high resolution - achieving high transmission amplitude through a large inner waveguide width and reduced wall thickness, (3) low surface roughness - its smooth surface minimises THz scattering, and (4) high electrical conductivity - ensuring high radiation efficiency with minimal energy loss[62,63]. The 3D-printed ODS Cu in this work can significantly advance 6 G communication with its smooth surface, sub-100 µm resolution, high strength, and high conductivity. Thus, our work represents a very promising solution for achieving the desired geometry complexity with microscale features for high-performance THz antennas in a facile manufacturing process.

Discussion

A facile 3D-printable ODS Cu strategy was developed by introducing nanoscale Cu_2O strengthening particles via in-situ oxidation during the gas atomisation stage. This facile ODS strategy can be readily implemented by fine-tuning the oxygen content in the gas atomisation process, resulting in controlled formation of modified Cu_2O particles. The AMed ODS Cu exhibits a multiscale grain and sub-grain microstructure with high-density, well-dispersed nanoparticles, leading to a high yield strength of 450 MPa and an electrical conductivity of 80% IACS. Additionally, ultrafine feature sizes as small as ~70 µm and nanoscale surface roughness were achieved due to increased laser absorptivity, higher melt viscosity, and a unique dynamic wetting transition at high and low temperatures. In the future, the ODS strategy may extend its application in Cu alloys to enhance printing resolution and overall performance. As a demonstration case study, high-resolution ODS Cu was used in the PBF-LB process to fabricate a THz micro-architected antenna with significantly improved performance, showing great potential for future telecommunication applications.

Methods

Fabrication process

The ODS Cu and pure Cu powders were manufactured through a modified VIGA method (Supplementary Text 1 and Supplementary Fig. 14). Details of the ODS Cu and pure Cu powders are provided in Supplementary Table 4, which presents the particle size distribution, packing density, apparent density, and flowability data for both ODS Cu and pure Cu powders. The data demonstrate that these properties are at a comparable level for both ODS Cu and pure Cu. The morphologies of both powders were characterised (Supplementary Fig. 15). The ODS Cu components were fabricated using a self-developed PBF-LB system, i.e., Han's Laser M100µ. The machine configurations are listed in Supplementary Table 5. Pure Cu was used as the substrate material. Bars with dimensions of 2 mm × 2 mm × 30 mm were used in the electrical conductivity test, and disc-shaped cylinders with a diameter of 12.7 mm and thickness of 2.5 mm were used for the thermal conductivity test. Cubes with dimensions of 5 mm × 5 mm × 5 mm were characterised through optical microscopy and EBSD to obtain the morphologies of the as-printed samples. Dog-bone samples with gauge dimensions of 10 mm × 2 mm × 1.5 mm were machined through wire-electrode cutting.

Microstructural characterisation

The laser reflectivity of the pure Cu and ODS Cu powders was measured by the UV-Visible-NIR Lambda 950 PerkinElmer spectrophotometer, equipped with a 150 mm integrating sphere, operating within the wavelength range of 400–2000 nm. The viscosity of the pure Cu and ODS Cu powders was measured by high-temperature viscometer, *BCT1700*, using oscillating-cup method within the temperature range of 1373–1873 K. The contact angle of pure Cu and ODS Cu at high temperatures is obtained a DataPhysics optical contact angle measuring instrument. The particle distribution is measured by the laser diffraction particle size analyser, *Bettersize*, China. The microstructures of initial powders were analysed using scanning electron microscope (SEM, JCM-6000Plus). The optical-microscopic characteristics were examined using an RH-2000 high-resolution 3D microscope (Hirox). The samples underwent grinding, polishing, and etching processes using an etching solution composed of 5 g $FeCl_3$, 85 mL ethanol, and 15 mL HCl. The crystal structure was analysed using an EBSD system (EDAX Velocity Plus) with a step size of 0.2 µm and scan area of 500 µm × 500 µm. The EBSD data were analysed using MTEX 5.7.0, an open-source MATLAB toolbox. High-resolution microstructure analysis was performed using TEM (JEOL JEM 2100 F). Needle-shaped specimens for atom probe tomography (APT) were fabricated using lift-outs and annular milling techniques with an FEI Scios focused-ion beam/SEM. APT characterisations were performed using a CAMEACA LEAP 5000 XR local electrode atom probe. The samples were analyzed in voltage mode at a temperature of 70 K, employing a pulse repetition rate of 200 kHz, a pulse fraction of 20%, and an evaporation detection rate of 0.2% atoms per pulse. The AP Suite 6.1 software was employed to generate 3D reconstructions and

analyse the acquired data. The phase validation of samples was calculated using XRD patterns obtained using a high-resolution Rigaku SmartLab X-ray diffractometer, with a 2θ angle range of 20° to 100°. The step size was 0.02°, and the scan speed was 0.1°/min. Tensile tests were conducted on tensile bars at a constant speed of 0.6 mm/min. Electrical conductivity was assessed with a micro-ohmmeter with an accuracy of 0.05% and a sensitivity of 1 μΩ. Thermal conductivity was assessed using a light flash apparatus (LFA467, NETZSCH) at 25 °C. Electrical and thermal conductivity measurements were performed on three samples to ensure consistency and repeatability. Prior to evaluating the mechanical performance and the electrical and thermal conductivity properties, the samples were subjected to grinding and polishing to mitigate any errors associated with rough surfaces. The as-printed cubic lattice specimens were subjected to quasi-static compression tests using an MTS universal tester at a strain rate of ~10^{-3} s^{-1}, And the tests were terminated upon densification. The tensile test samples of gauge dimension 15 × 4 × 1.5 mm^3 were machined by wire-electrode cutting. Tensile tests were conducted under quasi-static speed at a strain rate of 10^{-3} s^{-1}. Mechanical tests were conducted on the three samples fabricated with each parameter set.

In-situ SXRD tensile experiments were conducted on the FAST beamline at the Cornell High Energy Synchrotron Source (CHESS) utilising an X-ray energy of 51.996 KeV (λ = 0.2384 Å). Two-dimensional (2D) X-ray diffraction patterns were obtained using transmission mode. from a 1 × 1.2 mm^2 (thickness × width) gauge section of the tensile specimen, using a Dual-panel Dexela 2923 detector positioned 600 mm behind the sample. Calibration of the sample-to-detector distance and instrumental broadening was performed using the CeO_2 NIST powder standard. Two-dimensional (2D) diffraction patterns were acquired at a nominal strain rate of ~5×10^{-4} s^{-1} and were integrated along specified azimuth angles to obtain one-dimensional (1D) diffraction patterns, which were subsequently analyzed with GSAS-II software[70]. The Pseudo-Voigt function was used for fitting single peaks to determine their positions, and the *hkl* plane-specific lattice strain for each phase was calculated by

$$\varepsilon_{hkl} = (d_{hkl} - d^0_{hkl})/d^0_{hkl} \tag{1}$$

where d^0_{hkl} and d_{hkl} are the reference lattice d-spacing in the stress-free condition and the lattice d-spacing during loading, respectively. Lattice strain is defined as the relative change in lattice spacing, averaged over a specific family of grains during loading, compared to the value at zero load[71].

High-fidelity thermal-fluid flow modelling

The melt pool dynamics are simulated with a high-fidelity thermal-fluid flow model. The fluid is assumed to be incompressible, laminar, and Newtonian. The equations governing mass, momentum, and energy conservation are:

$$\nabla \cdot (\rho \mathbf{v}) = 0 \tag{2}$$

$$\frac{\partial}{\partial t}(\rho \mathbf{v}) + \nabla \cdot (\rho \mathbf{v} \otimes \mathbf{v}) = -\nabla p + \nabla \cdot (\mu \nabla \mathbf{v}) + \mathbf{f}_B - D\rho \mathbf{v} \tag{3}$$

$$\frac{\partial}{\partial t}(\rho h_s) + \nabla \cdot (\rho \mathbf{v} h_s) = \nabla \cdot (k \nabla T) + q \tag{4}$$

where ρ represents the material density, $\mathbf{v}$ denotes the velocity vector, p stands for the pressure, μ indicates the viscosity, $\mathbf{f}_B$ is the buoyancy force evaluated using the Boussinesq approximation, and D is the Darcy drag force coefficient, as discussed in the ref. 72. The symbol k represents the thermal conductivity, T denotes the temperature, and $h_s = c_p T + (1 - f_s)L_m$ is the specific enthalpy, where c_p, f_s and L_m are the specific heat, solid fraction, and latent heat of melting, respectively. The symbol q is the power absorbed by the material, where a simplified Gaussian laser beam is applied:

$$Q(x,y) = \frac{APN}{2\pi R_b} \exp\left[-N \cdot \left(\frac{x^2 + y^2}{2R_b^2}\right)\right] \tag{5}$$

where A is the experimentally measured absorptivity, P denotes the laser power, $N = 4.6$ denotes the laser concentration coefficient, and R_b denotes the laser beam radius that encompasses 99% of the total power. The free surfaces are monitored using the Volume of Fluid (VoF) method,

$$\frac{\partial F}{\partial t} + \nabla \cdot (F\mathbf{v}) = 0 \tag{6}$$

where F denotes the fluid fraction. The thermal boundary condition and pressure p_s on the free surface of the melt pool are

$$-k\nabla T \cdot \mathbf{n} = h(T - T_s) + \varepsilon\sigma_s\left(T^4 - T_s^4\right) + m_{loss}L \tag{7}$$

$$p_s = \sigma\kappa + P_{rec}(T) \tag{8}$$

where $\mathbf{n}$ is the normal vector to the surface, h represents the convective heat transfer coefficient, ε is the emissivity coefficient, $\sigma_s = 5.67 \times 10^{-8} Wm^{-2}K$ is the Stefan-Boltzmann constant, $T_s = 298K$ represents the ambient temperature and m_{loss} represents the mass loss due to evaporation. In the pressure equation, κ is the curvature of the free surface, and $P_{rec}(T)$ is the recoil pressure. The surface tension of copper, σ under the influence of oxygen is elaborated in Supplementary Text 7. The estimation of the thermal conductivity of the liquid ODS Cu is elaborated in Supplementary Text 8. The material properties of Cu and ODS Cu used in the simulation are listed in Supplementary Table 6. In the simulation, the copper base with initial temperature of 298 K has dimensions (in mm) of 0.7 (L) × 0.4 (W) × 0.5 (D). Variable meshing strategy was used to save computation time, and the mesh size is 3 μm in the volume of interest (which contains the entire melt pool).

Transmit-array antenna design and experimental analysis

The transmit-array antenna and waveguide element were simulated using the finite element method module in the ANSYS High-Frequency Simulation software module. The transmission performance of the waveguide element was evaluated in the periodic boundary condition to replicate an infinite array scenario. Moreover, the radiation performance was assessed through full-wave simulations, in which the transmit-array and feed horn were placed in two vacuum boxes with the finite element and boundary integral condition. A wave port was designated at the end of the horn for excitation. The frequency range was set as 140–220 GHz, with a central frequency of 150 GHz. The focus-to-diameter-ratios (F/D) of the transmit-array was set as 1.6, where D is the dimension of the transmit-array (33.6 mm in this study).

Experiments were conducted in an anechoic chamber, as shown in Fig. 6B. Radiation patterns were obtained using a vector network analyser (VNA) (N5242B), designed for frequencies ranging from 10 MHz to 26.5 GHz. The measurement range was extended to 140–220 GHz using a pair of frequency extender modules (V05VNA2-T/R) from OML Inc. A horn (SGH-05) from Millitech was used as the feed source for radiating THz waves to the transmit-array. The holder was 3D printed to maintain the distance between the transmit-array and phase centre of the horn at 53.8 mm. The transmit-array manipulated the phase distribution and generated a high-gain beam in free space. Another horn (SGH-05) was mounted to a robotic arm as the receiver. The radiation pattern was captured by rotating the robotic arm with an angular step of 1°.

The gain of the transmit-array antenna was calculated using the gain-comparison method[73]. First, the received power during the radiation pattern measurement was recorded as P_1. Subsequently, the transmit-array antenna was replaced by a standard horn (SGH-05) with a known gain G_s. In this configuration, the received power was measured as P_2. The gain of the transmit-array antenna, G_T, was calculated as follows:

$$G_T(dB) = G_s(dB) + P_1(dBm) - P_2(dBm) \quad (9)$$

Data availability

The data supporting the findings of this study are available within the article and its supplementary information. Source data are provided with this paper.

References

1. Johnson, K. et al. A copper pyramidal fractal antenna fabricated with green-laser powder bed fusion. *Prog. Addit. Manuf.* **7**, 931–942 (2022).
2. Hirt, L., Reiser, A., Spolenak, R. & Zambelli, T. Additive manufacturing of metal structures at the micrometer scale. *Adv. Mater.* **29**, 1604211 (2017).
3. Gao, S., Ding, J., Qu, S., Liu, H. & Song, X. Numerical and experimental investigation of additively manufactured shell-lattice copper heat exchanger. *Int. Commun. Heat. Mass Transf.* **147**, 106976 (2023).
4. Gao, S. et al. Additive manufacturing of alloys with programmable microstructure and properties. *Nat. Commun.* **14**, 6752 (2023).
5. Todaro, C. J. et al. Grain structure control during metal 3D printing by high-intensity ultrasound. *Nat. Commun.* **11**, 142 (2020).
6. Li, Z. et al. Enhanced strengthening and hardening via self-stabilized dislocation network in additively manufactured metals. *Mater. Today* **50**, 79–88 (2021).
7. Liu, Y. et al. Manufacturing of high strength and high conductivity copper with laser powder bed fusion. *Nat. Commun.* **15**, 1283 (2024).
8. Liu, Y. et al. Laser powder bed fusion of copper matrix iron particle reinforced nanocomposite with high strength and high conductivity. *J. Mater. Sci. Technol.* **134**, 50–59 (2023).
9. Tertuliano, O. A. et al. High absorptivity nanotextured powders for additive manufacturing. *Sci. Adv.* **10**, eadp0003, https://doi.org/10.1126/sciadv.adp0003.
10. Qu, S. et al. High-precision laser powder bed fusion processing of pure copper. *Addit. Manuf.* **48**, 102417 (2021).
11. Hu, D., Qu, S., Ding, J., Song, X. & Fu, M. W. Size effect on the mechanical behaviours of pure copper sheet-based triply periodic minimal surface structures fabricated by micro-laser powder bed fusion. *J. Manuf. Process.* **127**, 736–749 (2024).
12. Davis, J. R. *Copper and copper alloys* (ASM international, 2001).
13. Kini, A. R. et al. In-situ synthesis via laser metal deposition of a lean Cu–3.4Cr–0.6 Nb (at%) conductive alloy hardened by Cr nano-scale precipitates and by Laves phase micro-particles. *Acta Mater.* **197**, 330–340 (2020).
14. Rittinghaus, S.-K. & Wilms, M. B. Oxide dispersion strengthening of γ-TiAl by laser additive manufacturing. *J. Alloy. Compd.* **804**, 457–460 (2019).
15. Wilms, M. B. & Rittinghaus, S.-K. Laser additive manufacturing of oxide dispersion-strengthened copper–chromium–niobium alloys. *J. Manufact. Mater. Process.* **6**, https://doi.org/10.3390/jmmp6050102 (2022).
16. Baitimerov, R. M. & Bykov, V. A. Processing of alumina reinforced copper metal matrix composite by selective laser melting technology. *Solid State Phenom.* **316**, 175–180 (2021).
17. Song, T. et al. Strong and ductile titanium–oxygen–iron alloys by additive manufacturing. *Nature* **618**, 63–68 (2023).
18. Doñate-Buendia, C. et al. Microstructure formation and mechanical properties of ODS steels built by laser additive manufacturing of nanoparticle coated iron-chromium powders. *Acta Mater.* **206**, 116566 (2021).
19. Smith, T. M. et al. A 3D printable alloy designed for extreme environments. *Nature* **617**, 513–518 (2023).
20. Gu, R. N. et al. Intentional oxidation and laser remelting of highly reflective pure Cu for its high-quality additive manufacturing. *Adv. Eng. Mater.* **25**, 2101138 (2023).
21. Jadhav, S. D. et al. Influence of carbon nanoparticle addition (and Impurities) on selective laser melting of pure copper. *Materials* **12**, https://doi.org/10.3390/ma12152469 (2019).
22. Haines, M. P., Peter, N. J., Babu, S. S. & Jägle, E. A. In-situ synthesis of oxides by reactive process atmospheres during L-PBF of stainless steel. *Addit. Manuf.* **33**, 101178 (2020).
23. Rombouts, M., Kruth, J. P., Froyen, L. & Mercelis, P. Fundamentals of selective laser melting of alloyed steel powders. *CIRP Ann.* **55**, 187–192 (2006).
24. Dong, Z., Ma, Z., Yu, L. & Liu, Y. Achieving high strength and ductility in ODS-W alloy by employing oxide@W core-shell nanopowder as precursor. *Nat. Commun.* **12**, 5052 (2021).
25. Wilms, M. B., Rittinghaus, S.-K., Goßling, M. & Gökce, B. Additive manufacturing of oxide-dispersion strengthened alloys: Materials, synthesis and manufacturing. *Prog. Mater. Sci.* **133**, 101049 (2023).
26. García, V. G., Cabrera, J. M. & Prado, J. M. Role of Cu2O during hot compression of 99.9% pure copper. *Mater. Sci. Eng.: A* **488**, 92–101 (2008).
27. Si, C., Tang, X., Zhang, X., Wang, J. & Wu, W. Characteristics of 7055Al alloy powders manufactured by gas-solid two-phase atomization: a comparison with gas atomization process. *Mater. Des.* **118**, 66–74 (2017).
28. Wang, G. et al. Enhanced plasticity due to melt pool flow induced uniform dispersion of reinforcing particles in additively manufactured metallic composites. *Int. J. Plasticity* **164**, 103591 (2023).
29. Zhang, Q. et al. CuO nanostructures: synthesis, characterization, growth mechanisms, fundamental properties, and applications. *Prog. Mater. Sci.* **60**, 208–337 (2014).
30. Pham, M.-S., Dovgyy, B., Hooper, P. A., Gourlay, C. M. & Piglione, A. The role of side-branching in microstructure development in laser powder-bed fusion. *Nat. Commun.* **11**, 749 (2020).
31. Kaur, J., Khanna, A., Kumar, R. & Chandra, R. Growth and characterization of Cu2O and CuO thin films. *J. Mater. Sci.: Mater. Electron.* **33**, 16154–16166 (2022).
32. MacDonald, E. & Wicker, R. Multiprocess 3D printing for increasing component functionality. *Science* **353**, aaf2093 (2016).
33. Metelkova, J. et al. On the influence of laser defocusing in Selective Laser Melting of 316 L. *Addit. Manuf.* **23**, 161–169 (2018).
34. Lee, N. & Cho, H. H. Thermal design of operating parameter for reliable AlSi7Mg selective laser melting. *J. Mater. Res. Technol.* **30**, 4405–4411 (2024).
35. Sahoo, P., Debroy, T. & McNallan, M. J. Surface tension of binary metal—surface active solute systems under conditions relevant to welding metallurgy. *Metall. Trans. B* **19**, 483–491 (1988).
36. Qu, M. et al. Controlling process instability for defect lean metal additive manufacturing. *Nat. Commun.* **13**, 1079 (2022).
37. Bidare, P., Bitharas, I., Ward, R. M., Attallah, M. M. & Moore, A. J. Fluid and particle dynamics in laser powder bed fusion. *Acta Mater.* **142**, 107–120 (2018).
38. Diemer, M., Neubrand, A., Trumble, K. P. & Rödel, J. Influence of oxygen partial pressure and oxygen content on the wettability in the copper–oxygen–alumina system. *J. Am. Ceram. Soc.* **82**, 2825–2832 (1999).

39. Dou, T. et al. The influence of FeCoCrNi HEA porous coating on dynamic wetting and spreading behaviors of AlSi alloy on steel substrate by laser irradiation. *J. Manuf. Process.* **125**, 38–49 (2024).
40. Xu, W. et al. Dynamic wetting and spreading mechanisms regulated by elemental Ni in a Mg/steel immiscible system during laser processing. *J. Manuf. Process.* **80**, 600–611 (2022).
41. Liu, Q. et al. High-strength and high-conductivity additively manufactured Cu-O alloy enabled by cellular microstructure. *Addit. Manuf.* **88**, 104244 (2024).
42. Jadhav, S. D. et al. Surface modified copper alloy powder for reliable laser-based additive manufacturing. *Addit. Manuf.* **35**, 101418 (2020).
43. Jadhav, S. D., Goossens, L. R., Kinds, Y., Hooreweder, B. V. & Vanmeensel, K. Laser-based powder bed fusion additive manufacturing of pure copper. *Addit. Manuf.* **42**, 101990 (2021).
44. Wang, J., Zhou, X. & Li, J. Evolution of microstructures and properties of SLM-manufactured Cu–15Ni–8Sn alloy during heat treatment. *Addit. Manuf.* **37**, 101599 (2021).
45. Wang, J., Zhou, X. L., Li, J., Brochu, M. & Zhao, Y. F. Microstructures and properties of SLM-manufactured Cu-15Ni-8Sn alloy. *Addit. Manuf.* **31**, 100921 (2020).
46. Jadhav, S. D. et al. Modification of electrical and mechanical properties of selective laser-melted CuCr0.3 alloy using carbon nanoparticles. *Adv. Eng. Mater.* **22**, 1900946 (2020).
47. Tang, X. et al. A study on the mechanical and electrical properties of high-strength CuCrZr alloy fabricated using laser powder bed fusion. *J. Alloy. Compd.* **924**, 166627 (2022).
48. Jadhav, S. D., Vleugels, J., Kruth, J.-P., Van Humbeeck, J. & Vanmeensel, K. Mechanical and electrical properties of selective laser-melted parts produced from surface-oxidized copper powder. *Mater. Des. Process. Commun.* **2**, e94 (2020).
49. Zhang, S. et al. Microstructure and properties of high strength and high conductivity Cu-Cr alloy components fabricated by high power selective laser melting. *Mater. Lett.* **237**, 306–309 (2019).
50. Wallis, C. & Buchmayr, B. Effect of heat treatments on microstructure and properties of CuCrZr produced by laser-powder bed fusion. *Mater. Sci. Eng. A* **744**, 215–223 (2019).
51. Wang, Q. et al. Effect of process parameters and heat treatment on the microstructure and properties of CuCrZr alloy by selective laser melting. *Mater. Sci. Eng. A* **857**, 144054 (2022).
52. Xu, S. et al. Improving strength and elongation combination of Cu–9Ni–6Sn-(0.2 Nb) alloys by pre-annealing and aging treatment. *Mater. Sci. Eng. A* **860**, 144221 (2022).
53. Ventura, A. P. et al. The effect of aging on the microstructure of selective laser melted Cu-Ni-Si. *Metall. Mater. Trans. A* **48**, 6070–6082 (2017).
54. Huang, J. et al. Pure copper components fabricated by cold spray (CS) and selective laser melting (SLM) technology. *Surf. Coat. Technol.* **395**, 125936 (2020).
55. Lin, T.-C. et al. Aluminum with dispersed nanoparticles by laser additive manufacturing. *Nat. Commun.* **10**, 4124 (2019).
56. Chen, L.-Y. et al. Processing and properties of magnesium containing a dense uniform dispersion of nanoparticles. *Nature* **528**, 539–543 (2015).
57. Ghosh, S. et al. Quantitative prediction of yield strength of highly alloyed complex steel using high energy synchrotron X-ray diffractometry. *J. Mater. Res. Technol.* **20**, 485–495 (2022).
58. Xu, R. et al. A review of broadband low-cost and high-gain low-terahertz antennas for wireless communications applications. *IEEE Access* **8**, 57615–57629 (2020).
59. Zhu, S. Y., Li, Y. L., Luk, K. M. & Pang, S. W. Compact high-Gain Si-Imprinted THz antenna for ultrahigh speed wireless communications. *IEEE Trans. Antennas Propag.* **68**, 5945–5954 (2020).
60. Deng, X. D., Li, Y., Wu, W. & Xiong, Y. Z. 340-GHz SIW cavity-backed magnetic rectangular slot loop antennas and arrays in silicon technology. *IEEE Trans. Antennas Propag.* **63**, 5272–5279 (2015).
61. Wu, G. B., Zeng, Y. S., Chan, K. F., Qu, S. W. & Chan, C. H. High-Gain circularly polarized lens antenna for terahertz applications. *IEEE Antennas Wirel. Propag. Lett.* **18**, 921–925 (2019).
62. Nayeri, P. et al. 3D printed dielectric reflectarrays: low-cost high-gain antennas at sub-millimeter waves. *IEEE Trans. Antennas Propag.* **62**, 2000–2008 (2014).
63. Gu, C. et al. A D-Band 3D-Printed antenna. *IEEE Trans. Terahertz Sci. Technol.* **10**, 433–442 (2020).
64. He, Y., Chen, Y., Zhang, L., Wong, S. W. & Chen, Z. N. An overview of terahertz antennas. *China Commun.* **17**, 124–165 (2020).
65. Wu, G. B., Zeng, Y. S., Chan, K. F., Qu, S. W. & Chan, C. H. 3-D printed circularly polarized modified fresnel lens operating at terahertz frequencies. *IEEE Trans. Antennas Propag.* **67**, 4429–4437 (2019).
66. Chahat, N. et al. 1.9-THz multiflare angle horn optimization for space instruments. *IEEE Trans. Terahertz Sci. Technol.* **5**, 914–921 (2015).
67. Fan, K., Hao, Z. C., Yuan, Q. & Hong, W. Development of a High Gain 325–500 GHz Antenna Using Quasi-Planar Reflectors. *IEEE Trans. Antennas Propag.* **65**, 3384–3391 (2017).
68. Miao, Z. W. et al. A 400-GHz high-gain quartz-based single layered folded reflectarray antenna for terahertz applications. *IEEE Trans. Terahertz Sci. Technol.* **9**, 78–88 (2019).
69. You, J.-L. et al. Electroless plating of a 5 G copper antenna on polyimide patterned with laser-induced selective activation and curing of metal–organic catalyst. *Appl. Surf. Sci.* **599**, 153990 (2022).
70. Toby, B. H. E. X. P. G. U. I. a graphical user interface for GSAS. *J. Appl. Crystallogr.* **34**, 210–213 (2001).
71. An, K. et al. First in situ lattice strains measurements under load at VULCAN. *Metall. Mater. Trans. A* **42**, 95–99 (2011).
72. Wang, L., Zhang, Y., Chia, H. Y. & Yan, W. Mechanism of keyhole pore formation in metal additive manufacturing. *npj Comput/ Mater.* **8**, 22 (2022).
73. Balanis, C. A. *Antenna theory: analysis and design* (John Wiley & sons, 2016).

Acknowledgements

The authors acknowledge the financial support of the Hong Kong Special Administrative Region University Grants Committee - General Research Fund CUHK14209523 as well as Collaborative Research Fund C4002-22Y, C4074-22G and C7074-23G. W.C. acknowledges the faculty start-up support from the University of Southern California.

Author contributions

S.Q., L.W., and X.S. conceived the concept and designed the experiments. X.S., W.C., and Y.L. supervised the project. S.Q., L.W., S.Z., and C.Y. carried out the main experiments. H.C., Z.H., and W.Y. conducted the simulation. Y.Z. and J.D. contributed idea for the research. G.W., C.Y., and C.C. conducted the antenna experiment and data analysis. S.Z. and W.C. conducted the SXRD characterisation. S.Q., L.W., S.Z., C.Y., H.C., W.C., and X.S. wrote the manuscript. All authors contributed to the discussion of the data.

Competing interests

The authors declare no competing interests.

Additional information

Supplementary information The online version contains supplementary material available at https://doi.org/10.1038/s41467-025-58373-6.

Correspondence and requests for materials should be addressed to Wen Chen, Yang Lu or Xu Song.

Peer review information *Nature Communications* thanks Bilal Gökce, Jan Wegner, and the other, anonymous, reviewer(s) for their contribution to the peer review of this work. A peer review file is available.